

Hierarchical Boltzmann simulations and model error estimation



Manuel Torrilhon*, Neeraj Sarna

Center for Computational Engineering & Department of Mathematics, RWTH Aachen University, Germany¹

ARTICLE INFO

Article history:

Received 29 December 2016
 Received in revised form 12 April 2017
 Accepted 13 April 2017
 Available online 22 April 2017

Keywords:

Boltzmann equation
 Hermite-expansion
 Fluid mechanics
 Discontinuous Galerkin method

ABSTRACT

A hierarchical simulation approach for Boltzmann's equation should provide a single numerical framework in which a coarse representation can be used to compute gas flows as accurately and efficiently as in computational fluid dynamics, but a subsequent refinement allows to successively improve the result to the complete Boltzmann result. We use Hermite discretization, or moment equations, for the steady linearized Boltzmann equation for a proof-of-concept of such a framework. All representations of the hierarchy are rotationally invariant and the numerical method is formulated on fully unstructured triangular and quadrilateral meshes using an implicit discontinuous Galerkin formulation. We demonstrate the performance of the numerical method on model problems which in particular highlights the relevance of stability of boundary conditions on curved domains. The hierarchical nature of the method allows also to provide model error estimates by comparing subsequent representations. We present various model errors for a flow through a curved channel with obstacles.

© 2017 Elsevier Inc. All rights reserved.

1. Introduction

From the point of view of non-equilibrium thermodynamics there are two fundamentally different approaches to flow computations. The vast majority are based on fluid dynamic equations using the classical closure relations of Navier–Stokes and Fourier [17]. Sometimes these relations may be refined or extended [28,34], but those models still remain in the context of macroscopic field theories [27]. On the other hand, if one is interested in precise non-equilibrium predictions, typically the Boltzmann equation is solved for the velocity distribution function of the particles [7].

The differences of the approaches are evident both mathematically and numerically. There is the use of continuum fields, like flow velocity and temperature in fluid dynamics on the one side and the microscopic probability function of the particle velocities on the other. Often, the distribution function is considered the cost to pay for increased non-equilibrium accuracy. Still, engineering fields are the preferred variables in applications and only obtained indirectly by averaging the distribution function. Numerically, there exists a very rich literature on different methods how to solve partial differential equations of fluid dynamics, from Finite-Volume (FV) to Finite-Element (FE) methods [20,14], which are still further developed. These often deal with accurate representation of the fields and the handling of nonlinearities in the equations. The Boltzmann equation, on the other hand, is frequently solved by particle methods, like the direct simulation Monte-Carlo method [3],

* Corresponding author.

E-mail addresses: mt@mathcces.rwth-aachen.de (M. Torrilhon), sarna@mathcces.rwth-aachen.de (N. Sarna).

¹ Mathematics (CCES), Schinkelstr. 2, 52062 Aachen, Germany.

where a central issue is given by speed-up [15] and noise reduction [2]. Direct discretizations use basic ingredients of the FV- or FE-approaches [8], but most effort goes into the efficient computation of the collision integral [23,12].

It is interesting to note, that any numerical approach to solve the Boltzmann equation necessarily contains a numerical method for fluid dynamic equations in the asymptotic limit of small mean free paths (small Knudsen number). While this limit may not be the focus of a Boltzmann solution, it is reasonable to expect that a serious implementation of the Boltzmann equation for flow computations should at least exhibit the capability of a fluid dynamic flow solver. On the other hand computing flow based on fluid dynamic equations is usually challenged by model errors when applied to non-equilibrium flows. In many cases model errors dominate numerical discretization errors and estimating these errors in an efficient way becomes essential when judging the results for flow applications.

This paper aims at a *hierarchical simulation* approach for the Boltzmann equation with the properties:

- The discretization of the Boltzmann equation ranges from coarse to fine representations in a cascading hierarchy using a *single numerical framework*.
- The coarse representation should result in an *accurate and efficient* numerical method to solve the classical fluid dynamic equations within the single framework.
- The finer representations give a *valid and successively better* numerical discretization of the Boltzmann equation which allows high accuracy.
- All representations are *rotationally invariant* such that the numerical method can handle unstructured meshes and possibly complex geometries easily.
- The framework should provide a systematic for *model error estimation* between the different representations and allow model-refinement local in space.

To present a proof of concept for such a framework this paper will consider steady and slow processes (low Mach number) and thus linear equations. The main challenge is to find a formulation that can include both the hyperbolic nature of the Boltzmann transport process in the fine representation as well as the elliptic nature of the Stokes problem in the coarse representation. We use a Hermite-discretization which results in hyperbolic relaxation systems, known as moment equations [21,5], that are solved with a discontinuous Galerkin method [18]. The Hermite-discretization yields the classical fluid dynamic equations in a reformulated way which fit into the framework. Additionally, stable boundary conditions are an essential ingredient. The entropy estimate for the hyperbolic systems provides simple conditions to guarantee stability of boundary conditions [29,24] and we demonstrate and discuss the numerical impact of these conditions for several simplified model systems. We also show that the coarsest representation in the framework gives an accurate discretization to fluid dynamic equations.

The hierarchy of representations allows to quickly obtain model error estimates by comparing a result with the solution on the next finer level. To demonstrate this approach we will consider the flow through a curved channel with obstacles and efficiently estimate the local model error of a classical fluid dynamic simulation within the hierarchical Boltzmann framework. The local errors of finer representations can be estimated in an analogous way and an example is also given. Local model refinement and using different representations in different domains is left for future work.

The original idea of using moment equations for hierarchical simulations was formulated by Müller in the context of extended thermodynamics, see the text book [21]. The moment systems were introduced as ‘theory of theories’ in which the convergence behavior of subsequent systems was used to predict their validity. Both well-posed boundary conditions and suitable computational methods were not available so that the examples of extended thermodynamics were mostly simple cases.

Note that the requirement to have a valid discretization for fluid dynamic equations on the coarsest level is similar to asymptotic preserving schemes [10]. However, in this paper no smallness parameter is involved, instead we demand that when reducing the numerical degrees of freedom for the Boltzmann discretization we literally arrive at a fluid dynamics implementation. The approach in [9] is similar in spirit, but lacks the cascading hierarchical setup.

The implementation of the methods presented in this paper is freely available at the website GitHub [36]. This code not only is capable to produce the simulation results presented, but also contain the explicit details of the large system matrices and analytical solutions used. In this way the code complements the information of this paper.

2. Hermite-discretization for the Boltzmann equation

We consider the Boltzmann equation for monatomic ideal gases in the form

$$\frac{\partial f}{\partial t} + c_i \frac{\partial f}{\partial x_i} = S(f) \quad (1)$$

where $S(f)$ is the collision operator. The Maxwell distribution

$$f_M(\mathbf{c}; \rho, \mathbf{v}, \theta) = \rho/m(2\pi\theta)^{-3/2} \exp\left(-\frac{(c_i - v_i)(c_i - v_i)}{2\theta}\right) \quad (2)$$

based on a local density ρ , macroscopic velocity \mathbf{v} , and temperature θ is an equilibrium point of the Boltzmann equation in the sense that $S(f_M) = 0$. The particle mass is given by m .

Boundary conditions for walls are based on the accommodation model for the wall, which gives the incoming distribution as a superposition of a specularly reflected and an accommodated part which follow a given wall distribution function. We choose an outward-facing wall normal \mathbf{n} with a corresponding velocity component c_n and the wall does not move in the normal direction. The case of moving walls is left for future work. We denote by f_{wall} the distribution function of the particles accommodated with the wall and f is the distribution of the gas just in front of the wall. The distribution function f at the wall is then given by

$$f(\mathbf{c})|_{\text{BC}} = \begin{cases} \chi f_{\text{wall}}(\mathbf{c}) + (1 - \chi) f(\mathbf{c}^*) & c_n < 0 \\ f(\mathbf{c}) & c_n > 0 \end{cases} \quad (3)$$

where the velocity reflection \mathbf{c}^* inverts the sign of the component normal to the wall c_n .

2.1. Steady linear equations

We will discretize the steady Boltzmann equation by a Hermite expansion in velocity space, see also [16,4,33,5]. In the framework of this paper we will use an expansion based on a fixed Maxwellian $f_M(\mathbf{c}; \rho_0, \mathbf{0}, \theta_0)$ corresponding to an equilibrium ground state with density ρ_0 , velocity $\mathbf{v}_0 = \mathbf{0}$ and temperature θ_0 . An extension to the non-linear case is planned as future work. The distribution then takes the form

$$f_N(\mathbf{x}, \mathbf{c}) = \sum_{n=0}^{N_d} \sum_{s=0}^{M_n} w_{i_1 i_2 \dots i_n}^{(s)}(\mathbf{x}) \psi_{i_1 i_2 \dots i_n}^{(s)}\left(\frac{\mathbf{c}}{\theta_0^{1/2}}\right) f_M(\mathbf{c}; \rho_0, \mathbf{0}, \theta_0) \quad (4)$$

with deviatoric (tracefree) coefficients $w_{i_1 i_2 \dots i_n}^{(s)}(\mathbf{x})$ depending on space \mathbf{x} and derived from basis functions $\psi_{i_1 i_2 \dots i_n}^{(s)}(\mathbf{c}/\theta_0^{1/2})$. The highest tensor degree is N_d and M_n is the number of radial or trace coefficients on tensor level n . It could be shown in [26] that such a spectral expansion does converge to the solution of a kinetic equation in the linear case and we assume convergence for the scenarios presented in this paper.

In the expansion, the sum in n and s is explicit, but additionally doubled indices $i_k \in \{1, 2, 3\}$ are summed over (summation convention). Different choices of upper limits of the sums represent different discretization levels or representations. The basis functions read

$$\psi_{i_1 i_2 \dots i_n}^{(s)}(\boldsymbol{\xi}) = \xi_{i_1} \xi_{i_2} \dots \xi_{i_n} p_s^{(n)}\left(\frac{\boldsymbol{\xi}^2}{2}\right) \quad (5)$$

where the tensor $\xi_{i_1} \xi_{i_2} \dots \xi_{i_n}$ is a fully symmetric and deviatoric (tracefree) tensor of n -th degree that can be constructed by

$$\xi_{i_1} \xi_{i_2} \dots \xi_{i_n} = \frac{(-1)^n}{(2n-1)!!} \|\boldsymbol{\xi}\|^{2n+1} \frac{\partial^n}{\partial \xi_{i_1} \partial \xi_{i_2} \dots \partial \xi_{i_n}} \left(\frac{1}{\|\boldsymbol{\xi}\|} \right) \quad (6)$$

or alternatively through recursive constructions of traces. As a result, the n -th degree tracefree tensor $\xi_{i_1} \xi_{i_2} \dots \xi_{i_n}$ contains in total $2n+1$ independent components which can be written as linear combinations of $2n+1$ spherical harmonic functions at level n , modeling the anisotropy of the distribution function. On each level n of anisotropy the radial dependence is modeled by the polynomials

$$p_s^{(n)}(y) = \sum_{m=0}^s (-1)^m \frac{\Gamma(n+s+\frac{3}{2})}{\Gamma(n+m+\frac{3}{2})} \binom{s}{m} y^m \quad (7)$$

which are related to associated Laguerre polynomials. The basis functions (5) are orthogonal such that the expansion (4) satisfies

$$\tilde{w}_{i_1 i_2 \dots i_n}^{(s)}(\mathbf{x}) := n! s! \frac{\Gamma(n+s+\frac{3}{2})}{\Gamma(n+\frac{3}{2})} \rho_0 w_{i_1 i_2 \dots i_n}^{(s)}(\mathbf{x}) = m \int_{\mathbb{R}^3} \psi_{i_1 i_2 \dots i_n}^{(s)}\left(\frac{\mathbf{c}}{\theta_0^{1/2}}\right) f_N(\mathbf{x}, \mathbf{c}) d\mathbf{c} \quad (8)$$

where the variables $\tilde{w}_{i_1 i_2 \dots i_n}^{(s)}(\mathbf{x})$ absorb the normalizing constants in order to provide more compact expressions below. The variables \tilde{w} can easily be related to fluid dynamic quantities. Due to the fixed ground state it is reasonable to consider perturbations \hat{U} of an equilibrium ground state U_0 for all fluid variables such that $U = U_0 + \hat{U}$. When only linear contributions of the perturbations \hat{U} are considered, the variables \tilde{w} represent the following fluid quantities

$$\tilde{w}^{(0)} = \rho_0 + \hat{\rho}, \quad \tilde{w}_i^{(0)} = \rho_0 \frac{\hat{v}_i}{\theta_0^{1/2}}, \quad \tilde{w}^{(1)} = -\frac{3}{2} \rho_0 \frac{\hat{\theta}}{\theta_0}, \quad \tilde{w}_{ij}^{(0)} = \frac{\hat{\sigma}_{ij}}{\theta_0}, \quad \tilde{w}_i^{(1)} = -\frac{\hat{q}_i}{\theta_0^{3/2}} \quad (9)$$

where $\hat{\sigma}_{ij}$ is the stress tensor and \hat{q}_i is the heat flux of the gas.

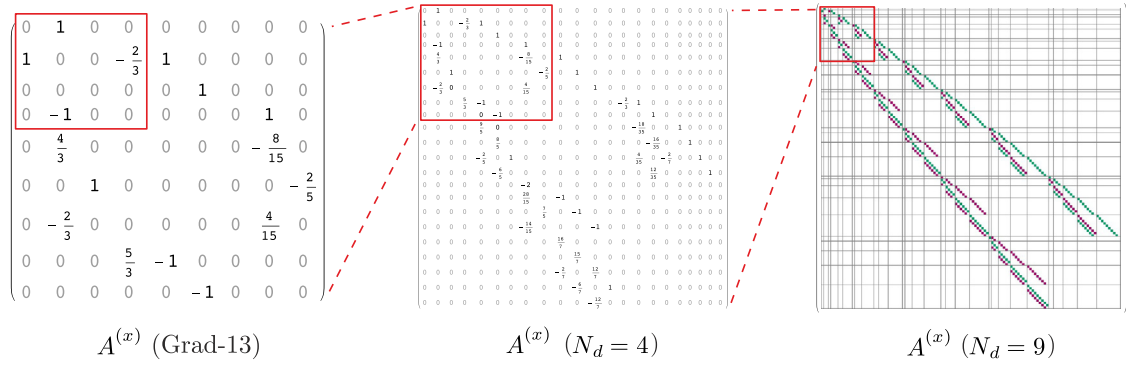


Fig. 1. Example of a cascade for system matrices of Hermite-discretizations for the Boltzmann equation.

The expansion (4) is inserted into the Boltzmann equation (1) and the equation is then projected onto the basis functions (5). We follow [21,33] and use recursion formulas for Laguerre polynomials and deviatoric tensors to transform the Boltzmann equation into the system of partial differential equations for $\tilde{w}_{i_1 i_2 \dots i_n}^{(s)}(\mathbf{x})$

$$\frac{2n}{2n+1} \left(\frac{2n+2s+1}{2} \partial_{i_1} \tilde{w}_{i_2 i_3 \dots i_n}^{(s)} - \partial_{i_1} \tilde{w}_{i_2 i_3 \dots i_n}^{(s+1)} \right) + \partial_k \tilde{w}_{i_1 i_2 \dots i_n k}^{(s)} - s \partial_k \tilde{w}_{i_1 i_2 \dots i_n k}^{(s-1)} = \theta_0^{-1/2} P_{i_1 i_2 \dots i_n}^{(s)} \quad (10)$$

with $n = 0, \dots, N_d$ and $s = 0, \dots, M_n$ for each n . In this paper we will mostly use discretizations considering complete tensors such that $M_n = \lfloor (N_d - n)/2 \rfloor$ with Gauss brackets $\lfloor \cdot \rfloor$. Two other popular choices are $N_d = 1$ and $M_n \in \{1, 0\}$ which represents the (linear) Euler equations with variables $\{\rho, v_i, \theta\}$ and Grad's 13-moment-case with $N_d = 2$ and $M_n \in \{1, 1, 0\}$ which adds stress and heat flux to the Euler equations. The equations of Navier–Stokes and Fourier follow from this case, see Sec. 5.4.

The production terms in (10) are based on the Boltzmann collision operator or an approximation. The paper uses Maxwell-molecules and applies the linear perturbation approximation as discussed above. This gives a diagonalized linear operator

$$P_{i_1 i_2 \dots i_n}^{(s)} = \int_{\mathbb{R}^3} \psi_{i_1 i_2 \dots i_n}^{(s)}(\mathbf{c}) S(f) d\mathbf{c} = -\frac{1}{\tau} a^{(s,n)} \tilde{w}_{i_1 i_2 \dots i_n}^{(s)} \quad (11)$$

on the right hand side of (10) with positive coefficients $a^{(s,n)}$, see [21,35] for details. It is easy to adjust this right hand side to BGK- or Shakov-models or the hard-sphere or other particle interactions [6]. Main parameter implied by the Boltzmann equation is the inverse collision frequency of relaxation time τ . A mean free path follows from the formula $\lambda = \theta_0^{1/2} \tau$ which may be used to define a Knudsen number λ/L with a macroscopic length L . In the next sections we will set $\theta_0 = 1$ and use τ synonymous to a Knudsen number.

The final Hermite-discretization of the Boltzmann equation (10) has the structure

$$A^{(x)} \partial_x U + A^{(y)} \partial_y U + A^{(z)} \partial_z U = -PU \quad (12)$$

with system matrices $A^{(x,y,z)}$ and production matrix P . The variable vector U combines the components of all coefficients \tilde{w} into a single vector. The system matrices can be identified from (10) with the help of computer algebra software, using properties of deviatoric tensors and selecting a set of independent components of the deviatoric variables $\tilde{w}_{i_1 i_2 \dots i_n}^{(s)}$. One advantage of Hermite-discretizations is rotational invariance of the equations such that no artifacts will be present for non-Cartesian settings. Additionally, subsequent increase of variables follow a hierarchical structure such that the system matrices are contained in each other. The smallest matrices represent fluid dynamic theories which means that the coarsest order of discretization will still give reasonable and highly efficient simulation results.

In the remainder of this paper we will consider the spatially two-dimensional situation, such that $\partial_z \equiv 0$. This also simplifies the tensor variables even though they formally remain tensor in three dimensions, since the velocity space remains three-dimensional. An example for the hierarchy of system matrices for a setup in two space dimensions is shown in Fig. 1. Only the matrices in x -direction are shown. The block marked in the outer left matrix is the system matrix of the Euler equations which is a subset of the 13-moment case, which itself is displayed as a subset of a matrix for a system using full tensors up to degree four. The outer right case uses $N_d = 9$ which results in a total of 125 variable components in two dimensions.

2.2. Wall boundary conditions

An alternative form of the kinetic boundary condition (3) can be found by splitting the distribution function f into an odd and even part with respect to the normal velocity c_n leading to the relation

$$f^{(\text{odd})} = \frac{\chi}{2 - \chi} \left(f_{\text{wall}} - f^{(\text{even})} \right) \quad \text{for } c_n < 0 \quad (13)$$

which defines the relevant incoming part of the distribution. For linear moment systems based on Hermite discretization boundary conditions are required for those components of the coefficients $\tilde{w}_{i_1 i_2 \dots i_n}^{(s)}$ which are odd in $\mathbf{c} \cdot \mathbf{n}$ in the coordinate system of the boundary [16,37]. If these components belong to the basis function components $\psi^{(\text{BC})}(\mathbf{c})$ the wall boundary conditions follow from the projection

$$\int_{c_n < 0} \psi^{(\text{BC})} f_N^{(\text{odd})} d\mathbf{c} = \frac{\chi}{2 - \chi} \left(\int_{c_n < 0} \psi^{(\text{BC})} f_{\text{wall}} d\mathbf{c} - \int_{c_n < 0} \psi^{(\text{BC})} f_N^{(\text{even})} d\mathbf{c} \right) \quad (14)$$

where $f_N^{(\text{odd})}$ contains all components of the expansion (4) odd in $\mathbf{c} \cdot \mathbf{n}$ and $f_N^{(\text{even})}$ all even components. Consequently, after integration the left and right hand side of (14) contains the odd and even tensor components of the coefficients $w_{i_1 i_2 \dots i_n}^{(s)}$ when written in the wall normal frame.

The wall distribution is given by a Maxwellian of the form (2) but evaluated with a wall temperature $\theta^{(W)}$, a wall velocity $\mathbf{v}^{(W)}$ with $\mathbf{n} \cdot \mathbf{v}^{(W)} = 0$ and a wall density $\rho^{(W)}$ which follows from a zero mass flux condition for the wall. In the following we will use $V_t = v_t - v_t^{(W)}$ for the tangential slip velocity at the wall and $\Delta\theta = \theta - \theta^{(W)}$ for the temperature jump.

The final equations for the coefficients $w_{i_1 i_2 \dots i_n}^{(s)}$ are obtained from (14) together with (4) using computer algebra software. The resulting matrices also show hierarchical structure.

3. Stability of boundary conditions

Considering the generic system (12) we assume the variable vector is of length N such that $U \in \mathbb{R}^N$ and $A^{(x)}, A^{(y)}$ and P are $N \times N$ -matrices. It can be shown that the system can be symmetrized and, hence, is hyperbolic [21], that is, for a normal vector \mathbf{n} the matrix

$$A^{(n)} = n_x A^{(x)} + n_y A^{(y)} \quad (15)$$

is diagonalizable with real eigenvalues. In particular there are $p \leq N/2$ pairwise eigenvalues with negative and positive sign and p corresponding odd variable components. Consequently, we have p boundary conditions in the linearized form

$$B^{(n)} U = g \quad (16)$$

where $B^{(n)} \in \mathbb{R}^{p \times N}$ depending on the wall normal \mathbf{n} and g is the inhomogeneity induced by wall temperature and velocity.

3.1. Conditions for stability

It turns out to be important to study the stability of the boundary conditions (16) by considering the time dependent hyperbolic system

$$\partial_t U + A^{(x)} \partial_x U + A^{(y)} \partial_y U = 0 \quad (17)$$

which we assume to be in symmetric form, and homogeneous boundary conditions $B^{(n)} U = 0$ together with some smooth initial conditions. The L^2 -entropy on a bounded domain Ω should satisfy the equation

$$\frac{d}{dt} \int_{\Omega} \frac{1}{2} U(\mathbf{x}, t)^T U(\mathbf{x}, t) d\mathbf{x} = - \oint_{\partial\Omega} \frac{1}{2} U(\mathbf{x}, t)^T A^{(n)} U(\mathbf{x}, t) d\mathbf{x} \leq 0 \quad (18)$$

where $A^{(n)}$ from (15) is based on the boundary normal. Due to symmetric hyperbolicity $A^{(n)}$ is diagonalizable by $A^{(n)} = Q^T \Lambda Q$ with $\Lambda = \text{diag}(\Lambda_m, 0, \Lambda_p)$, where we combine the negative and positive eigenvalues in Λ_m and Λ_p , respectively. Moment equations are rotationally invariant and $\Lambda_m = -\Lambda_p$ holds. Note that Q will depend on the normal vector n of the boundary. Based on Q characteristic variables are defined by $W = QU$ with $W = (W_m, W_0, W_p)^T$. We now write the boundary conditions (16) with $g = 0$ in characteristic variables by transforming $B^{(n)} U = B^{(n)} Q^T W = (\tilde{B}_m \mid \tilde{B}_0 \mid \tilde{B}_p) W = 0$. Assuming \tilde{B}_m is invertible the last equation is solved for W_m yielding

$$W_m = (R_0, R_p) \begin{pmatrix} W_0 \\ W_p \end{pmatrix} \quad (19)$$

with $R_0 = -\tilde{B}_m^{-1} \tilde{B}_0$ and $R_p = -\tilde{B}_m^{-1} \tilde{B}_p$. This describes the boundary condition in characteristic form. The characteristic variables associated with the incoming waves W_m are described as function of the values of the outgoing and possibly

standing waves, W_p and W_0 . With this form of boundary conditions we can conclude for the boundary integral in (18) the condition

$$U^T A^{(n)} U = W^T \Lambda W = \begin{pmatrix} W_0 \\ W_p \end{pmatrix}^T \begin{pmatrix} R_0^T \Lambda_m R_0 & R_0^T \Lambda_m R_p \\ R_p^T \Lambda_m R_0 & \Lambda_p + R_p^T \Lambda_m R_p \end{pmatrix} \begin{pmatrix} W_0 \\ W_p \end{pmatrix} \stackrel{!}{\geq} 0. \tag{20}$$

Because $\Lambda_m = -\Lambda_p$ and Λ_p is a positive definite matrix we find

$$(i) R_0 = 0 \quad (ii) \Lambda_p - R_p^T \Lambda_p R_p \text{ pos. semi-def.} \tag{21}$$

as stability conditions for the boundary conditions (16). This analysis is equivalent to the one in [11] for Friedrichs systems and more details are presented in [22].

3.2. Discussion

The first condition implies that the incoming waves may depend on the outgoing waves but not on the zero-waves which are at rest with respect to the wall. Otherwise, this standing waves could constantly feed into the entropy in (18) and stability is not assured. Since the zero-waves are related to the null-space of the flux matrix $A^{(n)}$ condition (i) can be equivalently reformulated as

$$(i)' \ker A^{(n)} \subset \ker B^{(n)} \tag{22}$$

directly as condition that couples $A^{(n)}$ with $B^{(n)}$. This condition is easy to check for instance for moment equations and boundary conditions based on the accommodation model. Since the boundary conditions (14) are typically derived independent of the moment equations and their flux matrix it is not surprising that condition (i)' is not met in the general case. We will show below that already for model systems the null space condition (i)' is crucial for convergence of a numerical discretization and in order to solve moment equations the accommodation boundary conditions for moments need to be adjusted to satisfy (i)', see [24]. This can be done by modifying the coefficients of the highest moment component resulting in the equation (14).

Condition (ii) gives a lower and upper bound for R_p , that is, how the incoming waves may depend on the outgoing waves. Obviously, $R_p = 0$ is a limiting case in which the incoming waves are set to zero and the entropy dissipation in (18) is negative due to outgoing waves $U^T A^{(n)} U = W_p^T \Lambda_p W_p$. On the other hand, R_p can not be too large, otherwise the negative sign in (ii) will overcome the positivity of Λ_p and positive definiteness will be lost. Condition (ii) will depend on the details of the boundary matrix $B^{(n)}$. For systems of moment equation the condition has to be checked on a case by case basis. All equations used in this work satisfy (ii).

The general hyperbolic system given in (12) is symmetric, therefore its convex entropy functional is given by $\frac{1}{2} U^T U$. So the inequality given in (18) means that we require the actual physical entropy flux at the wall to be positive. The same inequality was also derived in [24] for the linear regularized 13-moment equations using the second law of thermodynamics. Onsager relations are then enforced in [24] to modify the boundary conditions obtained from the usual moment projection of the Maxwell accommodation model in order to ensure thermodynamic stability. These conditions can be related to (21) and the modifications are equivalent to the ones suggested below. A more detailed investigation of the relation between well-posedness of boundary conditions for hyperbolic systems and Onsager boundary conditions is out of scope of this paper and will be presented elsewhere.

4. DG formulation

To solve a hyperbolic system of moment equations like (12) we employ a standard discontinuous Galerkin discretization [18]. Using $V(\mathbf{x})$ and $U(\mathbf{x})$ as test and ansatz functions, respectively, the variational form for a single element K reads

$$\int_K V(\mathbf{x})^T \mathbf{A} \cdot \text{grad } U(\mathbf{x}) \, d\mathbf{x} - \oint_{\partial K} V(\mathbf{x})^T A_-^{(n)} (U(\mathbf{x}) - U_{\tilde{K}}(\mathbf{x})) \, ds + \int_K V(\mathbf{x})^T P U(\mathbf{x}) \, d\mathbf{x} = 0 \tag{23}$$

where $\mathbf{A} = (A^{(x)}, A^{(y)})$. We used partial integration twice with the upwind numerical flux resulting in the splitting matrix

$$A_-^{(n)} = \frac{1}{2} (A^{(n)} - |A^{(n)}|) \tag{24}$$

which contains the incoming waves. \tilde{K} is the neighboring element, and $V(\mathbf{x})$ and $U(\mathbf{x})$ the test and ansatz functions. We will restrict ourselves to two spatial dimensions and use (bi-)linear and (bi-)quadratic triangular and quadrilateral elements.

It remains to specify how the boundary conditions (16) are incorporated into (23). At the boundary the values for the virtual “neighbor” $U_{\tilde{K}}$ in the boundary integral of (23) needs to be specified. Because we have only p boundary conditions for N variables, in general, only p variables or variable combinations can actually be prescribed at the boundary. We assume

there exists a so-called selector matrix $X \in \mathbb{R}^{N \times N}$ which selects those variables or variable combinations $V_{BC} \in \mathbb{R}^p$ that will be prescribed such that

$$V = \begin{pmatrix} V_{BC} \\ V_{\text{rest}} \end{pmatrix} = X^{-1}U \quad (25)$$

holds with $V_{\text{rest}} \in \mathbb{R}^{N-p}$. The boundary variables V_{BC} could be a suitable selection of components of U such that X is merely a permutation matrix. But V_{BC} could also be the incoming characteristic variables such that $X = Q^T$ as defined in Sec. 3.1.

Let X have the form $X = (X_{BC}|X_{\text{rest}})$ with $X_{BC} \in \mathbb{R}^{N \times p}$. The boundary conditions can be written

$$B^{(n)}U = B^{(n)}XV = B^{(n)}X_{BC}V_{BC} + B^{(n)}X_{\text{rest}}V_{\text{rest}} = g \quad (26)$$

which can be solved for V_{BC} if the selector X is chosen properly. In the virtual neighbor $U_{\tilde{K}}$ we replace the part \tilde{V}_{BC} with its value according to the boundary conditions evaluated on the value U of the interior element. The part \tilde{V}_{rest} we simply replace by the corresponding interior value V_{rest} which represents extrapolation. Then the difference in U in the boundary integral of (23) can be written

$$U - U_{\tilde{K}} = X(V - V_{\tilde{K}}) \quad (27)$$

$$= X_{BC}(V_{BC} - \tilde{V}_{BC}) + X_{\text{rest}}(V_{\text{rest}} - \tilde{V}_{\text{rest}}) \quad (28)$$

$$= X_{BC}(V_{BC} - (B^{(n)}X_{BC})^{-1}(-B^{(n)}X_{\text{rest}}V_{\text{rest}} + g)) \quad (29)$$

$$= X_{BC}(B^{(n)}X_{BC})^{-1}(B^{(n)}X_{BC}V_{BC} + B^{(n)}X_{\text{rest}}V_{\text{rest}} - g) \quad (30)$$

$$= X_{BC}(B^{(n)}X_{BC})^{-1}(B^{(n)}U - g). \quad (31)$$

In the variational formulation this expression results in a weak formulation of the boundary conditions (16). Due to the pre-factor based on the selector matrix X the boundary conditions are in general broadcasted onto all components of the system of equations.

The discretized system is assembled into sparse matrix format and finally solved by the sparse direct linear solver Pardiso [25]. For the Boltzmann Hermite-discretization we use as selector matrix X a permutation which selects the odd variable components in (14) as boundary variables V_{BC} .

5. Model problems

Before complete moment systems are solved it is instructive to investigate the performance and behavior of the numerical approach on smaller test problems.

5.1. System A

A simplified system that describes rarefied heat conduction in a rigid gas is given by

$$\left. \begin{aligned} \nabla \cdot \mathbf{q} &= f \\ \nabla \theta + \nabla \cdot \mathbf{R} &= -\frac{1}{\tau} \mathbf{q} \\ (\nabla \mathbf{q})_{\text{dev}} &= -\frac{1}{\tau} \mathbf{R} \end{aligned} \right\} \quad (32)$$

where θ is the temperature, \mathbf{q} is the heat flux vector and \mathbf{R} is a higher order flux tensor. The scalar source term f represents a heating. This system can be derived for example from Grad's 13-moment-equations when the gas is assumed to be at rest and stress-free. For $\mathbf{R} = 0$ in the second equation it reduces to a simple Poisson problem for temperature. For $\mathbf{R} \neq 0$ the system is equivalent to a Stokes–Darcy–Brinkmann problem. We consider the system and differential operator to be set in \mathbb{R}^3 , such that \mathbf{q} is a 3-dimensional vector and \mathbf{R} is a symmetric trace-free or deviatoric 3×3 matrix. Correspondingly, $(\cdot)_{\text{dev}}$ takes the symmetric deviatoric part of a tensor. However, in a two-dimensional simulation none of the fields depend on the z-coordinate and the only relevant components are

$$U = (\theta, q_x, q_y, R_{xx}, R_{xy}, R_{yy}) \in \mathbb{R}^6. \quad (33)$$

Using these variables the system matrices are given by

$$A^{(x)} = \begin{pmatrix} 0 & 1 & 0 & 0 & 0 & 0 \\ 1 & 0 & 0 & 1 & 0 & 0 \\ 0 & 0 & 0 & 0 & 1 & 0 \\ 0 & \frac{2}{3} & 0 & 0 & 0 & 0 \\ 0 & 0 & \frac{1}{2} & 0 & 0 & 0 \\ 0 & -\frac{1}{3} & 0 & 0 & 0 & 0 \end{pmatrix}, \quad A^{(y)} = \begin{pmatrix} 0 & 0 & 1 & 0 & 0 & 0 \\ 0 & 0 & 0 & 0 & 1 & 0 \\ 1 & 0 & 0 & 0 & 0 & 1 \\ 0 & 0 & -\frac{1}{3} & 0 & 0 & 0 \\ 0 & \frac{1}{2} & 0 & 0 & 0 & 0 \\ 0 & 0 & \frac{2}{3} & 0 & 0 & 0 \end{pmatrix} \tag{34}$$

which exhibit the eigenvalues $\lambda_i \in \{0, 0, \pm 1, \pm\sqrt{2}\}$. The system is not symmetric but can be easily symmetrized by applying the symmetric positive definite matrix

$$S = \text{diag}\left(1, \begin{pmatrix} 1 & 0 \\ 0 & 1 \end{pmatrix}, \begin{pmatrix} 2 & 0 & 1 \\ 0 & 2 & 0 \\ 1 & 0 & 2 \end{pmatrix}\right) \tag{35}$$

from the left. Note that this changes the eigenvalues of the system matrices. Alternatively, we can use a similarity transformation with $S^{1/2}$ to obtain a symmetric system with identical eigenvalues when written in transformed variables $S^{1/2}U$. We decide to work with the present form of the system such that the variables keep a simple physical interpretation.

The simplest physical wall boundary conditions reads

$$q_n = \theta - \theta_W, \quad R_{nt} = q_t \tag{36}$$

with a classical temperature jump condition and a higher order condition combining the tangential heat flux with its flux. θ_W is the wall temperature. The indices n and t denote tensor components in a coordinate system spanned by the boundary normal $\mathbf{n} = (n_x, n_y)$ and the tangent $\mathbf{t} = \mathbf{n}^\perp = (-n_y, n_x)$. The variable vector (33) can be transformed into the normal/tangential components by multiplying with the rotation matrix

$$T(n_x, n_y) = \text{diag}\left(1, \begin{pmatrix} n_x & n_y \\ -n_y & n_x \end{pmatrix}, \begin{pmatrix} n_x^2 & 2n_x n_y & n_y^2 \\ -n_x n_y & n_x^2 - n_y^2 & n_x n_y \\ n_y^2 & -2n_x n_y & n_x^2 \end{pmatrix}\right) \tag{37}$$

constructed from the normal \mathbf{n} . This matrix satisfies $T(n_x, n_y) T(n_x, -n_y) = id$, and we have also $T(n_x, -n_y) A^{(x)} T(n_x, n_y) = A^{(n)}$, which demonstrates the rotational invariance of the system.

Interestingly, the boundary conditions (36) turn out to be unstable, since they do not satisfy the null-space condition (22) as can be easily checked after identifying

$$B^{(x)} = \begin{pmatrix} 1 & -1 & 0 & 0 & 0 & 0 \\ 0 & 0 & 1 & 0 & -1 & 0 \end{pmatrix} \tag{38}$$

as boundary matrix in x-direction. To evaluate the stability condition (22) we consider the two null-vectors of $A^{(x)}$

$$\mathbf{v}^{(1)} = (0, 0, 0, 0, 0, 1), \quad \mathbf{v}^{(2)} = (-1, 0, 0, 1, 0, 0) \tag{39}$$

and evaluating $B^{(x)} \mathbf{v}^{(1,2)}$ shows that the second boundary condition satisfies the nullspace condition while the first one not. The ansatz

$$q_n = \theta - \theta^{(W)} + \kappa_1 R_{nn}, \quad R_{nt} = q_t \tag{40}$$

reveals that $\kappa_1 = 1$ is the only choice for stable boundary conditions. In general, the coefficients of θ and R_{nn} must be identical. Note, that the second condition in (21) is satisfied for both the unstable boundary condition (36) and the stable one (40) with $\kappa_1 = 1$.

We will test the effect of the unstable and stable boundary condition on the numerical method by considering a double cylinder domain

$$\Omega = \left\{ (x, y) \in \mathbb{R}^2 \mid r_0^2 \leq x^2 + y^2 \leq r_1^2 \right\} \tag{41}$$

with the parameters and heat source

$$r_0 = 1/2, \quad r_1 = 2, \quad \theta_0^{(W)} = 1, \quad \theta_1^{(W)} = 1/2, \quad f(x, y) = 2 - x^2 - y^2. \tag{42}$$

Using cylindrical coordinates for the differential operators in (32) it is possible to derive an analytical solution for this setup both with the stable and unstable boundary condition. Due to symmetry the temperature depends only on the radius r and is given by

$$\theta(r) = C_1 + C_2 \ln\left(\frac{r}{\tau}\right) + \frac{1}{\tau} \left(\frac{1}{16} r^4 - \frac{1}{2} r^2 - \frac{2}{3} \tau^2 r^2 \right) \tag{43}$$

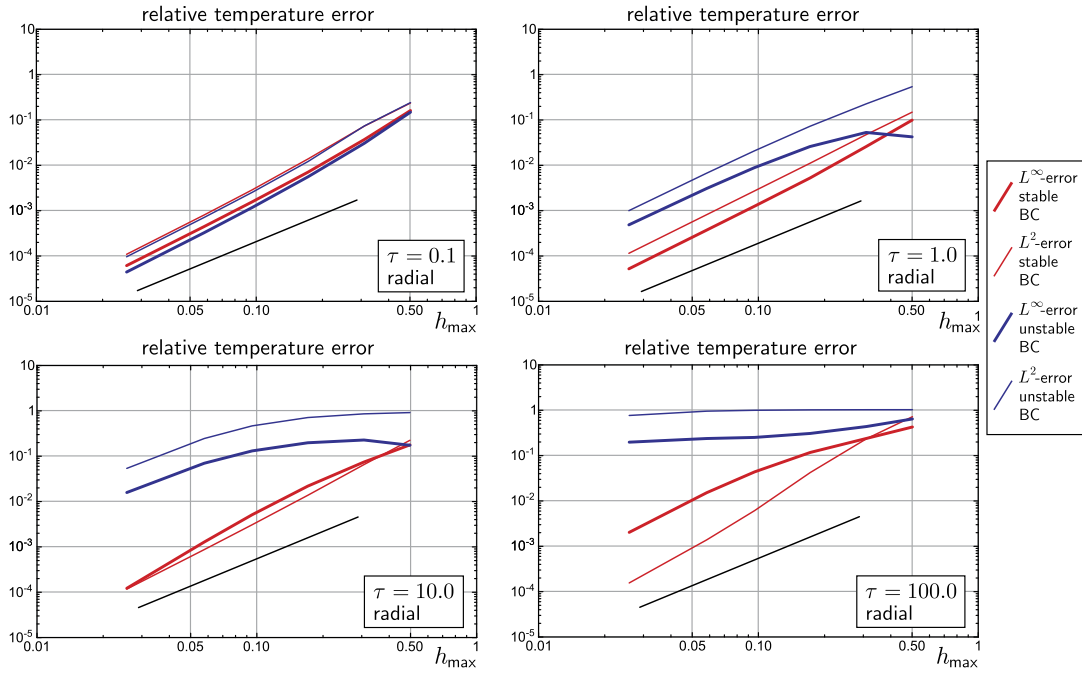


Fig. 2. Empirical convergence study for radial solution of model System A with stable (red) and unstable (blue) boundary conditions over a range of relaxation times τ . The solid black line gives second order as reference. (For interpretation of the references to color in this figure legend, the reader is referred to the web version of this article.)

with two integration constants $C_{1,2}$. In total the solution has four integration constants to be fixed by two boundary conditions both on the inner and outer cylinder. In order to be able to evaluate the temperature we give the values for $C_{1,2}$ for a set of relaxation times τ for the stable

stable BC's	$\tau = 0.1$	$\tau = 1.0$	$\tau = 10.0$	$\tau = 100.0$
C_1	-5.460256952	2.612851381	14.44110466	139.9358019
C_2	5.288321376	0.233772582	0.023497664	0.002482757

and unstable boundary condition

unstable BC's	$\tau = 0.1$	$\tau = 1.0$	$\tau = 10.0$	$\tau = 100.0$
C_1	-6.000111913	3.13888898	24.0469612	221.3469642
C_2	5.505007359	0.86140058	0.94960816	0.994396053

Note, that the main difference occurs for C_2 in the case $\tau = 100$.

We apply the discontinuous Galerkin approach (23) to the system (32) on a structured radial symmetric quadrilateral mesh with bi-linear elements. The boundary conditions are inserted on the odd variable components q_n and R_{nt} such that the selector matrix X as discussed in Sec. 4 is only a simple permutation. For simplicity the element error $e_K^{(\theta)}$ for temperature in element K is evaluated point-wise in the element centers and we then define the relative errors

$$L^\infty\text{-error} = \frac{\| \{e_K^{(\theta)}\}_{K \in \text{mesh}} \|_\infty}{\max\{\theta_K^{(\text{exact})}\}_{K \in \text{mesh}}}, \quad L^2\text{-error} = \frac{h_{\max} \| \{e_K^{(\theta)}\}_{K \in \text{mesh}} \|_2}{\max\{\theta_K^{(\text{exact})}\}_{K \in \text{mesh}}} \quad (44)$$

where h_{\max} is the maximal edge length of the mesh. The numerical results for different relaxation times $\tau \in \{0.1, 1.0, 10.0, 100.0\}$ are shown in Fig. 2. Each plot shows the errors for the unstable boundary conditions in blue and for the stable conditions in red. Both relative L^∞ - and L^2 -errors for temperature are shown. The gray line gives a reference curve for second order convergence. For $\tau = 0.1$ there is virtually no difference between the error curves. Indeed the difference of the analytical solutions is also small and in particular the value of R_{nn} , which makes the difference of the boundary conditions, is very small for small relaxation times. For increasing τ the errors for the unstable boundary conditions deteriorates and no convergence is visible in the case of $\tau = 100$. The stable boundary conditions consistently show second order convergence in agreement with the bi-linear elements. Note that for $\tau = 100$ the L^∞ -error is significant higher than the L^2 -error. This is due to small oscillation close to the wall. We will come back to this issue in Sec. 5.3.

5.2. System B

The system of Hermite discretizations exhibits a hierarchical structure where a low order system is contained in a higher order one. We will mimic this by adding an additional variable to System A and obtain

$$\left. \begin{aligned} \nabla \cdot \mathbf{q} &= f \\ \nabla\theta + \nabla \cdot \mathbf{R} &= -\frac{1}{\tau} \mathbf{q} \\ (\nabla \mathbf{q})_{\text{dev}} + \nabla \cdot \boldsymbol{\psi} &= -\frac{1}{\tau} \mathbf{R} \\ 2(\nabla \mathbf{R})_{\text{dev}} &= -\frac{1}{\tau} \boldsymbol{\psi} \end{aligned} \right\} \tag{45}$$

where $\boldsymbol{\psi}$ is a third degree deviatoric tensor. Note the structure of the equations of combining a gradient of a lower order with a divergence of a higher order variable. In two dimensions the essential set of components are

$$U = (\theta, q_x, q_y, R_{xx}, R_{xy}, R_{yy}, \psi_{xxx}, \psi_{xxy}, \psi_{xyy}, \psi_{yyy}). \tag{46}$$

System matrices, symmetrizer and rotation matrices for normal coordinates have a similar structure as in System A. We consider the system with the boundary conditions

$$q_n = \theta - \theta^{(W)} + \kappa_1 R_{nn}, \quad R_{nt} = q_t - v^{(W)} + \kappa_2 \psi_{nnt}, \quad \psi_{nnn} = R_{nn}, \quad \psi_{ntt} = R_{tt} \tag{47}$$

where the higher order conditions follow the structure of combining the normal flux of a variable with the tangential part of the variable as suggested from the kinetic boundary conditions. We have two boundary inhomogeneities given by $\theta^{(W)}$ and $v^{(W)}$. The two coefficients $\kappa_{1,2}$ will be used to control stability. Note that $v^{(W)} = 0$ and $\kappa_2 = 0$ corresponds to the case of System A in (40).

It is instructive to ask how the extension of the system affects the stability of the boundary conditions and the performance of the numerical method. Indeed, in case of the enlarged system the null-space condition (22) changes and it turns out that the boundary condition for the temperature jump in (47) is stable independent of κ_1 . However, the boundary condition for R_{nt} is influenced by the null-space condition which requires $\kappa_2 = 2$, or the coefficient of ψ_{nnt} being the double of the coefficient of q_t . Inspection of the analytical solutions unveils that in case of radial symmetry the fields of q_t and R_{nt} are trivially zero and, hence, the crucial unstable boundary condition is not active. We will demonstrate the stability of the first boundary condition for a radial symmetric test case and investigate the instability for an angular solution.

Radial test case: As above, we consider the double cylinder geometry (41) and the parameters (42), together with $v^{(W)} \equiv 0$ and κ_2 arbitrary. The analytical solution is now given by

$$\theta(r) = C_1 + C_2 \ln\left(\frac{r}{\tau}\right) + C_3 K_0\left(\lambda_2 \frac{r}{\tau}\right) + C_4 \left(I_0\left(\lambda_2 \frac{r}{\tau}\right) - 1\right) + \frac{1}{\tau} \left(\frac{1}{16} r^4 - \frac{1}{2} r^2 - \frac{2}{3} \tau^2 r^2\right) \tag{48}$$

where I_0 and K_0 are modified Bessel functions of first and second kind. These describe layer modes of the solution and come with integration constants related to the higher order boundary conditions. The inhomogeneous part of the temperature remains unchanged. The values of the integration constants for two cases of relaxation times are given by

	"stable"		"unstable"		
	$\tau = 0.1$	$\tau = 100.0$	$\tau = 0.1$	$\tau = 100.0$	
C_1	-5.540170055	266.8818134	C_1	-5.72829680	267.1129464
C_2	5.312471905	$8.71180699 \times 10^{-4}$	C_2	5.391875027	$1.43734302 \times 10^{-3}$
C_3	-18.6043756	$-3.6386886 \times 10^{-4}$	C_3	-18.8512861	$-6.1268167 \times 10^{-4}$
C_4	9.12125×10^{-9}	3.194759×10^6	C_4	9.11005×10^{-9}	3.1950059×10^6

where "stable" corresponds to $\kappa_1 = 1$ and "unstable" to $\kappa_1 = 0$ in (47) in accordance to the investigation of System A.

The upper row of Fig. 3 shows the empirical errors for temperature for System B obtained in the same manner as in Fig. 2 for $\tau = 0.1$ and $\tau = 100.0$. There is hardly any difference between both cases of boundary conditions which is due to stability of the boundary conditions independent of κ_1 in contrast to System A. The small difference is only due to different solutions that are to be approximated.

Angular test case: In order to see the influence of the unstable boundary condition we will construct a solution with angular dependence on the double cylinder geometry. The boundary inhomogeneity v_W and an angular dependent heat source is chosen to be

$$v_0^{(W)} = 5, \quad v_1^{(W)} = 0, \quad f(r, \varphi) = \left(-\frac{2}{5} + \frac{r^2}{9\tau^2}\right) \cos(\varphi) \tag{49}$$

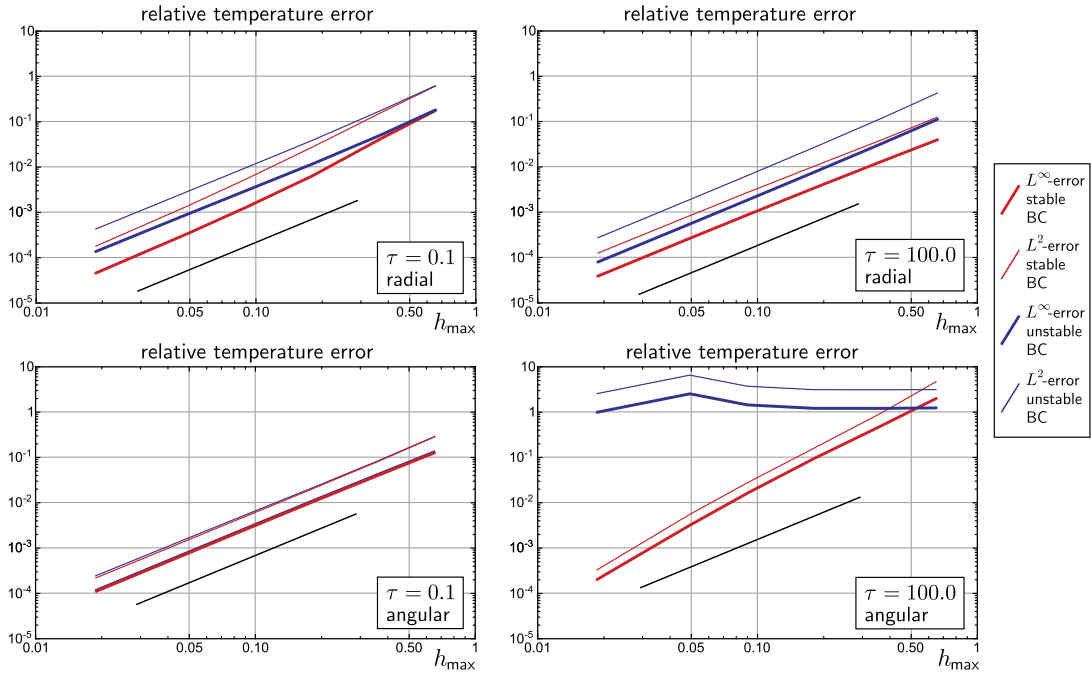


Fig. 3. Empirical convergence study of radial (top) and angular (bottom) solutions of model system (B) with stable (red) and unstable (blue) boundary conditions. The solid black line gives second order as reference. (For interpretation of the references to color in this figure legend, the reader is referred to the web version of this article.)

while $\theta^{(W)} \equiv 0$ and κ_1 can be arbitrary. The analytical solution for temperature now reads

$$\theta(r, \varphi) = \left(C_1 \frac{1}{r} + C_2 r + C_3 K_1(\lambda_2 r) + C_4 I_1(\lambda_2 r) + \frac{1}{\tau^3} \left(\frac{28}{135} r^2 \tau^2 - \frac{1}{135} r^4 \right) \right) \cos(\varphi) \tag{50}$$

where I_1 and K_1 are again Bessel functions. The values for the integration constants are given for two cases. The unstable case uses $\kappa_2 = 0$ and the stable case uses $\kappa_2 = 2$ in (47)

stable	$\tau = 0.1$	$\tau = 100.0$	unstable	$\tau = 0.1$	$\tau = 100.0$
C_1	-111.1391694	$-3.5152617 \times 10^{-5}$	C_1	-113.6011896	4.4663663×10^{-4}
C_2	6.6605695353	-5.3008490×10^3	C_2	6.6659777373	4.13783136×10^4
C_3	-68.42914074	1.3936541×10^{-5}	C_3	-7.145508969	$-3.2425996 \times 10^{-4}$
C_4	-1.54674×10^{-7}	1.1607281×10^4	C_4	-1.543674×10^{-7}	-9.0825262×10^4

Fig. 3 shows the numerical errors for the angular setup in the lower row. The non-convergence for the unstable boundary conditions in case of large relaxation times is clearly visible and follows the same pattern as for System A.

We conclude that the stability of boundary conditions will be crucial when solving large systems of moment equations.

5.3. Different grids and higher order

Before we solve moment equations it is interesting to consider the influence of different mesh types and higher order to steady hyperbolic problems of the type (12) with boundary conditions (16). As an example system we will re-use System B in (45) and the double cylinder geometry (41). The angular solution with parameters (49) serves as a non-trivial test-problem. In that case the stable boundary conditions are given by (47) with $\kappa_2 = 2$. We use Gmsh [13] to generate meshes of different type, namely structured quads, unstructured quads and unstructured triangles and the MOAB library [30] to handle the mesh in the DG implementation. Example grids of these three types are displayed in Fig. 4. Refined grids have not been obtained by cell division but re-generated by Gmsh with a smaller element size factor.

On quadrilateral meshes the DG method (23) has been employed with bi-linear Q_1 - and bi-quadratic Q_2 -elements, while the triangular meshes use linear P_1 - and quadratic P_2 -elements. Note, that the quadratic elements are formally capable to show third order of convergence. However, in our case the boundary of all meshes will be given by a polygonal approximation to the circular geometry for simplicity. Hence, higher than second order convergence will not be possible.

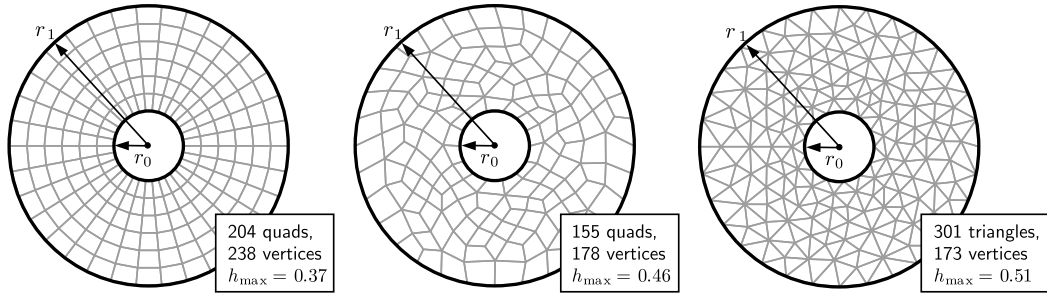


Fig. 4. Example meshes for a double cylinder geometry with $r_0 = 0.5$ and $r_1 = 2.0$ obtained with gmsh.

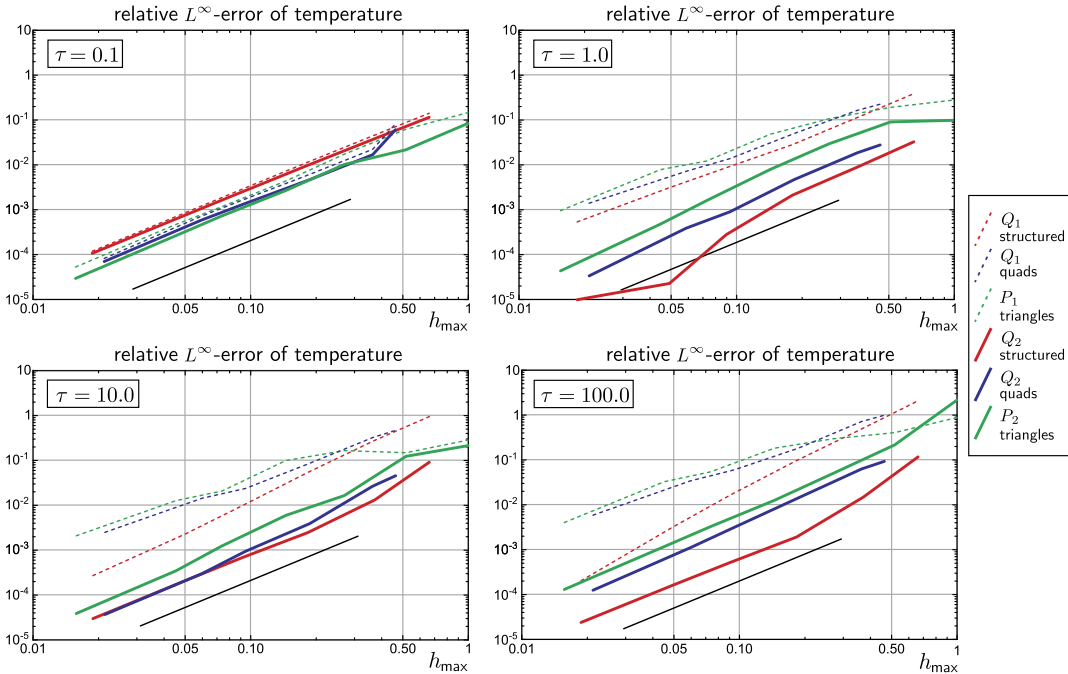


Fig. 5. Empirical convergence study for model system (B) on structured, unstructured quadrilateral, and triangular grids. The solid black line gives second order as reference.

The empirical errors for the angular solution of System B are shown in Fig. 5. The figure shows the relative L^∞ -error (44) of temperature for four different relaxation times $\tau \in \{0.1, 1.0, 10.0, 100.0\}$. Each plot shows the results for linear (dashed) and quadratic (solid) elements on structured, quadrilateral and triangular grids. All error curves show essentially second order convergence in agreement with the polygonal domain used. For small relaxation times the element order and grid regularity have no influence and the error shows the same level for all elements. For increasing relaxation times the curves separate. The higher order methods show a significant improvement of the error constant in comparison with linear methods. Inspection of the actual solutions shows that the quadratic elements are performing better especially at the boundary where small oscillations are further suppress in comparison to the linear results. We conclude that high order is beneficial even on a polygonal domain when computing solutions for larger relaxation times. Note that due to a scaling argument larger relaxation times are equivalent to a two-cylinder geometry with smaller radii. Hence, geometries with stronger curvature may also benefit from higher order.

As expected the structured mesh shows the smallest errors, while unstructured triangular and quadrilateral meshes perform comparably. Overall, different grids do not influence the error as much as the order of the elements.

The results show a decent performance for the DG method applied to moment-type system of equations. Further investigations, e.g., on grids with iso-parametric elements for better boundary approximation or p -adaptivity towards stronger curvature, are left for future work.

5.4. Fluid dynamic case

As next step, we will consider small realistic systems obtained from the Boltzmann discretization (10) that describe fluid dynamic equations. When choosing the variable vector

$$U = (\rho, v_x, v_y, \theta, \sigma_{xx}, \sigma_{xy}, \sigma_{yy}, q_x, q_y) \quad (51)$$

with density ρ , velocity components v_x, v_y , temperature θ , stress tensor components $\sigma_{xx}, \sigma_{xy}, \sigma_{yy}$ and heat flux components q_x, q_y , the moment system (10) gives the steady linear 13-moment-equations in the form

$$\begin{aligned} \rho_0 \partial_j \tilde{v}_j &= 0 \\ \theta_0 \partial_i \tilde{\rho} + \rho_0 \partial_i \tilde{\theta} + \partial_j \tilde{\sigma}_{ij} &= 0 \\ \rho_0 \theta_0 \partial_j \tilde{v}_j + \partial_j \tilde{q}_j &= 0 \\ \frac{4}{5} \partial_{(i} \tilde{q}_{j)} + 2\rho_0 \theta_0 \partial_{(i} \tilde{v}_{j)} &= -\frac{1}{\tau} \tilde{\sigma}_{ij} \\ \theta_0 \partial_j \tilde{\sigma}_{ij} + \frac{5}{2} \rho_0 \theta_0 \partial_i \tilde{\theta} &= -\frac{1}{\tau} \frac{2}{3} \tilde{q}_i \end{aligned} \quad (52)$$

where we will set the background values ρ_0, θ_0 to unity by proper scaling. If we drop the underlined terms, the last two equations turn into the laws of Navier–Stokes for stress tensor and Fourier’s law for heat flux. This NSF-system can be written in the generic form (12) with system matrix $A^{(x)}$ given by

i	1	2	2	2	3	4	4	5	6	7	8
j	2	1	4	5	6	2	8	2	3	2	4
$A_{ij}^{(x)}$	1	1	1	1	1	1	1	$\frac{4}{3}$	1	$-\frac{2}{3}$	$\frac{5}{2}$

(53)

in sparse triplet format. As in the case of the model systems it is possible to derive an explicit analytical solution for the NSF system on the double cylinder geometry (41). At the inner cylinder we use the simple jump and slip boundary conditions

$$v_n = 0, \quad q_n = \tilde{\chi} \Delta\theta, \quad \sigma_{nt} = \tilde{\chi} V_t \quad (54)$$

with simplified accommodation factor $\tilde{\chi} = 1$ and parameters $\theta^{(W)} = 1$ and $v_t^{(W)} = 0$. The outer cylinder provides a finite domain, but is a somewhat artificial interface mostly for numerical purposes. We model this outer cylinder as inflow/outflow boundary, but will use boundary conditions which are as close as possible to the standard wall conditions (54). In fact, we will only modify the first equation in (54) and replace it by

$$\gamma(v_n - v_n^{(W)}) = \tilde{\chi}(p - p^{(W)} + \sigma_{nn}) \quad (55)$$

which mimics the boundary conditions for heat flux and temperature and satisfies the null-space condition (22). A value $\gamma = 0$ allows to enforce pressure boundary conditions such that $p^{(W)} = p + \sigma_{nn}$ holds. In that case $v_n^{(W)}$ can be set arbitrarily, while $v_t^{(W)}$ must be prescribed in the last equation of (54). Alternatively, a limiting value $\gamma \rightarrow \infty$ allows to prescribe inflow conditions with $v_n = v_n^{(W)}$ and in this case $p^{(W)}$ is arbitrary. Note that inflow boundary conditions are often difficult because the flow may come with a non-equilibrium which is difficult to prescribe. Typically, initial layers are to be expected which adjust the artificial boundary value to the bulk. In the current test case this is not an issue because we can easily adjust the analytical solution to what ever is used in the numerical method. For the numerical method finite values for γ have a stabilizing effect and lead to better convergence behavior of the numerical method. We will use $\gamma = \varepsilon$ and $\gamma = 1/\varepsilon$ with $\varepsilon = 10^{-5}$ to model pressure and normal velocity boundary conditions on both cylinders.

For our example we assume the flow is driven by a pressure profile $p^{(in)} = -p_0 n_x$ along the outer circle with n_x the x -component of the outer normal vector. A temperature $\theta^{(in)} = 2$ is used at the outer cylinder. The velocity is set to $v_n^{(in)} = v_0 n_x$ and $v_t^{(in)} = -v_0 n_y$ with $v_0 = 1$. Inspection of the analytical solution shows that a pressure constant $p_0 = 0.23$ is consistent with a velocity $v_x \approx 1$ along the outer cylinder. An impression of the solution is given in Fig. 6.

The left plot of Fig. 7 shows the L^∞ -error of various fields of the Navier–Stokes–Fourier system (52) solved for flow and heat conduction between two cylinders at $\tau = 0.1$. The solid lines show the results for linear P_1 -elements on triangles. For comparison the results of bi-quadratic Q_2 -elements on a structured grid are also displayed with dashed lines. All fields including non-equilibrium quantities like stress and heat flux show second order convergence. As expected from the model systems higher order and structured grids give a better error constants, but at this relatively low relaxation time the difference is not significant.

The regularized 13-moment equations in steady first order, two-dimensional formulation are based on the 16 variables

$$U = (\rho, v_x, v_y, \theta, \sigma_{xx}, \sigma_{xy}, \sigma_{yy}, q_x, q_y, m_{xxx}, m_{xyy}, m_{xyy}, m_{yyy}, R_{xx}, R_{xy}, R_{yy}) \quad (56)$$

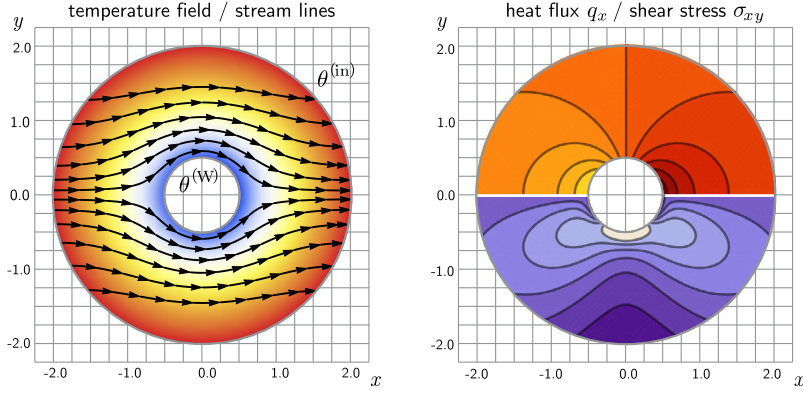


Fig. 6. Test case for the steady, linear Navier-Stokes-Fourier system with $\tau = 0.1$. Left: temperature field (colors between 1.32/blue and 1.92/red) with velocity stream lines. Right top: heat flux component q_x (contours from -0.236 to 0.236). Right bottom: shear stress component σ_{xy} (contours from -0.029 to 0.116). (For interpretation of the references to color in this figure legend, the reader is referred to the web version of this article.)

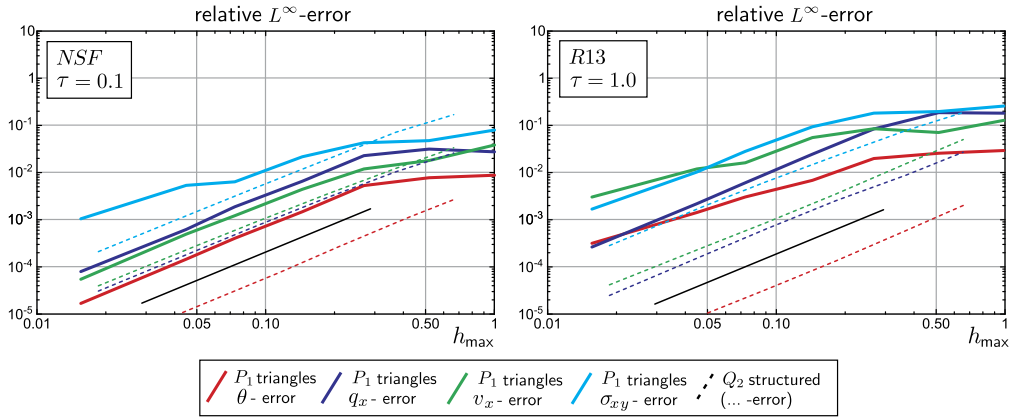


Fig. 7. Empirical error analysis for various field quantities of flow and heat conduction between two cylinders. Results for the NSF and R13 system on linear triangular elements and bi-quadratic structured quads. The solid black line gives second order as reference.

which include a third degree tensor m and an additional 2-tensor R . The additional scalar fourth degree moment Δ is identically zero in the present setting. The two additional variables enter the system (52) in the last two equations which now read

$$\partial_k \tilde{m}_{ijk} + \frac{4}{5} \partial_{(i} \tilde{q}_{j)} + 2\rho_0 \theta_0 \partial_{(i} \tilde{v}_{j)} = -\frac{1}{\tau} \tilde{\sigma}_{ij} \tag{57}$$

$$\partial_j \tilde{R}_{ij} + \theta_0 \partial_j \tilde{\sigma}_{ij} + \frac{5}{2} \rho_0 \theta_0 \partial_i \tilde{\theta} = -\frac{1}{\tau} \frac{2}{3} \tilde{q}_i \tag{58}$$

including the terms of the 13-moment equations. The constitutive equations for m and R read

$$3\theta_0 \partial_{(i} \tilde{\sigma}_{jk)} = -\frac{1}{\tau} \frac{3}{2} \tilde{m}_{ijk}, \quad \frac{28}{5} \theta_0 \partial_{(i} \tilde{q}_{j)} = -\frac{1}{\tau} \frac{7}{6} \tilde{R}_{ij} \tag{59}$$

and close the system. Consequently, the system matrices of the R13 equations include the values given in the table above, but add the following triplets

i	5	6	7	8	9	5	6	7	8	9	10	11	12	12	13	14	15	16
j	8	9	8	5	6	10	11	12	13	15	5	6	5	7	6	8	9	8
$A_{ij}^{(x)}$	$\frac{8}{15}$	$\frac{2}{5}$	$-\frac{4}{15}$	1	1	1	1	1	$\frac{1}{2}$	$\frac{1}{2}$	$\frac{9}{5}$	$\frac{8}{5}$	$-\frac{2}{5}$	1	$-\frac{6}{5}$	$\frac{56}{15}$	$\frac{14}{5}$	$-\frac{28}{15}$

which results in a 16×16 matrix with 29 non-zero entries. The R13 equations are solved on the double cylinder geometry in an identical setting as the NSF system above. Following the approach in [32,38] it is again possible to find an analytical

solution. The R13 system requires more boundary conditions which read

$$\begin{aligned}
 v_n &= 0, & q_n &= \tilde{\chi} \left(2\Delta\theta + \frac{1}{2}\sigma_{nn} + \frac{2}{5}R_{nn} \right), \\
 \sigma_{nt} &= \tilde{\chi} \left(V_t + \frac{1}{5}q_t + \underline{m_{ntt}} \right), & m_{nnn} &= \tilde{\chi} \left(-\frac{2}{5}\Delta\theta + \frac{7}{5}\sigma_{nn} - \frac{2}{25}R_{nn} \right) \\
 R_{nt} &= \tilde{\chi} \left(-V_t + \frac{11}{5}q_t - \underline{m_{ntt}} \right), & \frac{1}{2}m_{nnn} + m_{ntt} &= \tilde{\chi} \left(\frac{1}{2}\sigma_{nn} + \sigma_{tt} \right)
 \end{aligned} \tag{60}$$

where the underlined terms have been adjusted to satisfy the null-space condition (22). For the modification the following ad-hoc strategy has been adopted which has been used similarly in [24]. The null-space vectors of the system matrix have been computed and tested with the boundary matrix. For those conditions that give a non-vanishing result an ansatz has been used that changed only the coefficient of the largest moment in the equation. In this way the null-space condition implies a unique modification of the boundary conditions. The resulting boundary conditions (60) for R13 are identical to the Onsager boundary conditions in [24]. It could also be shown numerically that the condition (ii) in (21) holds.

The parameters of the inner and outer cylinder are identical to those used in the NSF case. In particular, we also replace the first condition in (60) by the inflow model (55) and use again $p^{(in)} = -p_0 n_x$. From the R13 analytical solution we find that $p_0 = 0.27$ is a consistent value for the pressure-driven inflow.

The L^∞ -error of various fields from the R13 simulation at $\tau = 1.0$ is shown in the right plot of Fig. 7. A similar behavior as in the NSF case can be observed. The difference in error constant between the linear triangular elements and the structured quadratic elements is more pronounced because of the larger value of the relaxation time. As discussed for the model system in Sec. 5.3 it might be necessary to use higher order at least near the boundary to achieve better errors on triangles.

6. Example channel flow with obstacles

The previous sections have introduced and tested a numerical approach to the generic system (12). We will now demonstrate the usefulness of the approach for full Hermite discretizations of the Boltzmann equation for more complex geometries and present a basic model error estimation approach. As a test case we consider a curved channel containing three obstacles, which combines aspects of realistic internal and external flows. Both the channel walls and the obstacles are given as smooth curves constructed from B-splines with the control points

$$\begin{aligned}
 \text{lower wall} &= \{(-2, 0), (0, 0), (0, -2)\} \\
 \text{upper wall} &= \{(-2, 1), (1, 1), (1, -2)\} \\
 \text{obstacle 1} &= \{(-1.4, 0.35), (-1, 0.5), (-0.6, 0.35), (-0.6, 0.6), (-1, 0.75), (-1.4, 0.75)\} \\
 \text{obstacle 2} &= \{(-0.1, -0.2), (0.25, -0.25), (0.4, -0.1), (0.1, 0), (-0.1, 0.3), (-0.4, 0.1)\} \\
 \text{obstacle 3} &= \{(0.55, -0.8), (0.2, -1.2), (0.6, -1.3), (0.8, -0.9), (0.7, -0.4), (0.5, -0.4)\}
 \end{aligned} \tag{61}$$

where the points for the obstacles are used in a periodic manner. The channel inflow and outflow boundaries are given by the lines $\{(0, -2), (1, -2)\}$, and $\{(-2, 0), (-2, 1)\}$. A sketch of the resulting geometry is presented in Fig. 8. The figure also displays the Gmsh-obtained triangular mesh which is used for the simulation results below, and some of its properties. The mesh has a refinement factor of three towards the obstacle walls. Quadratic P_2 -elements have been used in the entire domain for all simulations below. The flow is assumed to be pressure-driven from the lower to the upper channel end. Choosing the Knudsen number $Kn = 0.5$, – or a dimensionless relaxation time $\tau = 0.5$ in (12) – results in a channel inflow width of 2 mean free paths. Note that the setup contains features that give rise to much larger Knudsen numbers. For example, the channel width decreases next to the obstacles by a factor two to three, which gives a Knudsen number increased by the same factor. Also the tip of obstacle 3 may be used to define a Knudsen number up to 20-fold larger than based on the inflow width. We will assume Maxwell's accommodation model for all walls of the channel and the obstacle with identical temperature. As in the R13 case the boundary conditions for all moment models have been adjusted to satisfy the stability conditions (21) in such a way that only the coefficients of the highest moments are changed. Hence, in the hierarchy of models Maxwell's accommodation conditions are perfectly recovered in the limit of infinite moments. The inflow will be modeled as described in Sec. 5.4 with dimensionless inflow pressure $p_1 = 1$ and outflow pressure $p_0 = -1$. Note, that due to the linear nature of the equations the results will be proportional to $p_1 - p_0$. The focus of the investigation will be on the steady flow pattern and stress distribution.

The first simulation result is obtained by the Navier–Stokes–Fourier system (52) with first order jump and slip conditions. Due to linearity the flow solution is equivalent to that of a Stokes problem. The left hand side of Fig. 9 shows the flow lines and the contours of a stress tensor invariant of the Stokes result. The stress tensor invariant is given by

$$\sigma_v = \sqrt{\frac{3}{2}\sigma_{ij}\sigma_{ij}} = \sqrt{3(\sigma_{xx}^2 + \sigma_{xy}^2 + \sigma_{xx}\sigma_{yy} + \sigma_{yy}^2)} \tag{62}$$

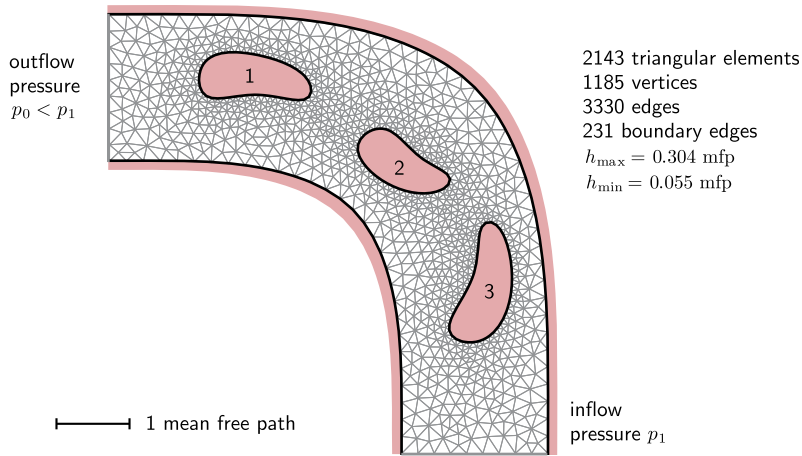


Fig. 8. Setup of a curved micro-channel with three obstacles. The flow is pressure driven and all walls are modeled based on full accommodation with the same temperature.

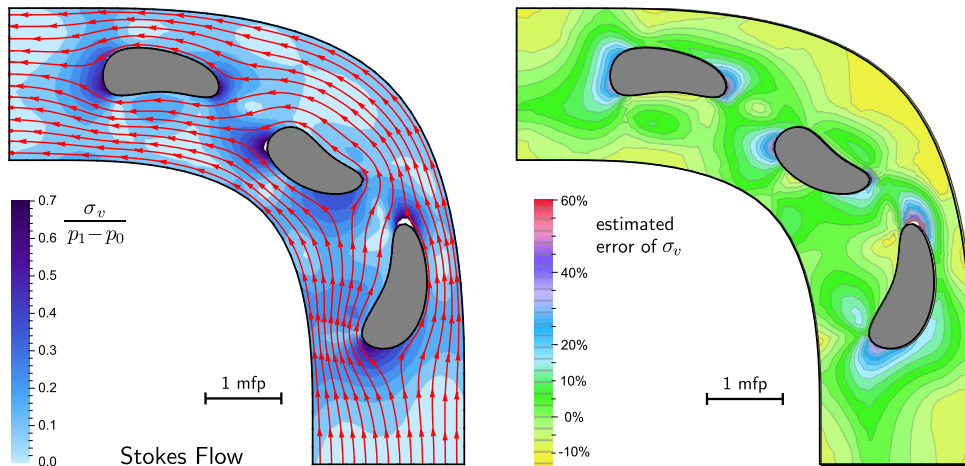


Fig. 9. Results for the channel flow obtained with the linear Navier–Stokes–Fourier system. Left: Stream lines are displayed with contours of the stress invariant σ_v . Right: relative error for stress invariant of Stokes estimated with a $N_d = 4(5)$ Boltzmann discretization. (For interpretation of the colors in this figure, the reader is referred to the web version of this article.)

also known as ‘equivalent tensile stress’ or ‘von-Mises stress’. It provides a useful reduction of the stress tensor to a scalar quantity. The stress invariant is scaled by the pressure difference that drives the channel. The stress shows a complicated pattern with high values at the tips and ends of the obstacles. Values beyond the given contour color scale are blanked out in white.

In order to estimate the model error present in the Stokes simulation we use a refined Hermite-discretization based on not only the NSF variables but include all components of the fourth ($N_d = 4$) and fifth coefficient tensor ($N_d = 5$) in (4). It is known that the Hermite expansion shows an oscillatory convergence behavior between odd and even approximation orders, see e.g., [21]. For this reason we will average the result of odd and even order and indicate the result by, e.g., $N_d = 4(5)$. A similar approach was used in [1,33,19]. If we use this result as an approximation to the true Boltzmann solution we can estimate the error of the Stokes simulation. The right hand side of Fig. 9 shows the estimated error of the stress invariant σ_v as a percentage after scaling with the global maximal value of stress observed in the simulation. Positive values represent an over-estimated and negative values an under-estimated stress. The classical fluid dynamic result mostly gives too large values for stress, with up to 60% error. Only the shear stress values at the channel walls are too small. It is typical for Boltzmann solutions to give more dissipation and thus lower stress levels than Stokes.

The left plot of Fig. 10 shows the stream lines and the stress invariant σ_v for the $N_d = 4(5)$ Boltzmann simulation, which was used to estimate the Stokes error. The stress contours are clearly different and close inspection also reveals some changes in the stream line behavior. Obviously, also the result of the Hermite discretization $N_d = 4(5)$ is based on

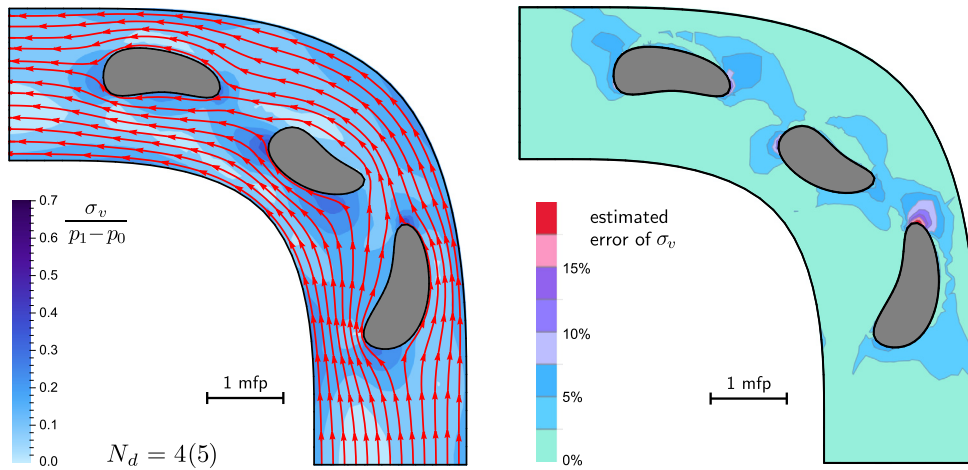


Fig. 10. Results for the channel flow obtained with the linear $N_d = 4(5)$ Boltzmann discretization. Left: Stream lines are displayed with contours of the stress invariant σ_v . Right: relative error for stress invariant of the left result estimated with a $N_d = 6(7)$ Boltzmann discretization. (For interpretation of the colors in this figure, the reader is referred to the web version of this article.)

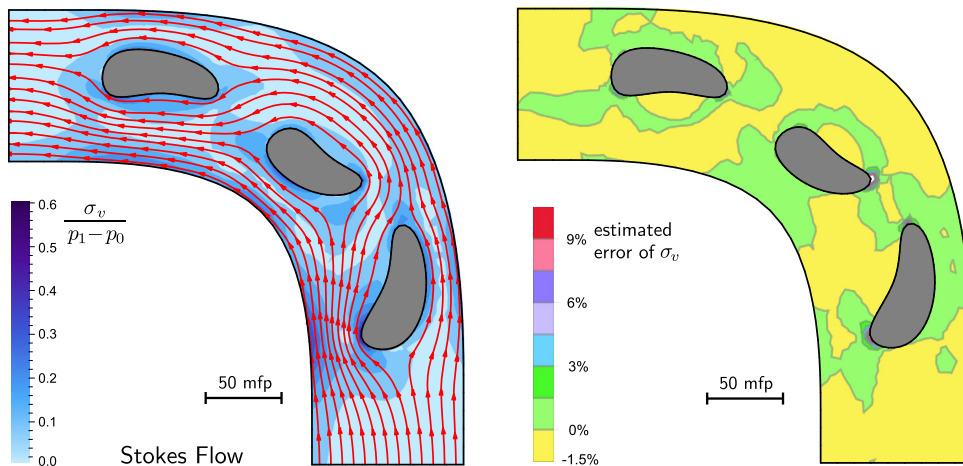


Fig. 11. Results for the channel flow obtained with the linear Navier-Stokes system for a small mean-free-path setting. Left: Stream lines are displayed with contours of the stress invariant σ_v . Right: relative error for the stress invariant of the left result estimated with a $N_d = 3(4)$ Boltzmann discretization. (For interpretation of the colors in this figure, the reader is referred to the web version of this article.)

an approximative model for the Boltzmann equation and affected by model errors. The hierarchical framework presented in this paper allows to estimate this error by considering a finer discretization. We use $N_d = 6(7)$ and compute the error in the analogous way as for the Stokes result. The contours on the right hand side of Fig. 10 show the relative estimated errors. Most of the domain now exhibit an error of only 2–5%. A remaining area with large errors is found at the top of obstacle 3. As discussed above this region also shows the largest value for the local Knudsen number due to the strongly curved boundary. To produce a reliable result for this region even finer Hermite-discretizations are needed, possibly in a locally adapted manner. The methods of this paper are ready for local model-refinement, but the investigation of such an approach is left for future work.

As we have seen the classical fluid dynamic model fails for the large Knudsen number scenario above. The model error is quickly detected by using a relatively coarse Boltzmann model while quantitative reliable results are obtained only by an even finer representation. It is instructive to investigate a lower Knudsen number case in which the gas in the channel is more dense or of less microscopic scale. Fig. 11 displays the simulation result for the channel with a 50 times smaller mean free path. The left hand side plot shows again the results of the Stokes equation with stress contours and stream lines. This can be directly compared to the left hand side of Fig. 9. Note, that the maximum stress value is now at a different place and also the stream lines are clearly different. However, this result can be estimated to be of very high accuracy. The right hand side shows the estimated model error based on a very coarse Boltzmann simulation with $N_d = 3(4)$. The majority of the channel domain shows error of $\pm 1.5\%$ and only very close to the obstacle tips the error grows to 5–15%. It now depends on the purpose of the simulation if these regions are of interest and a fine simulation is necessary.

To give some impression about the performance of the simulations we give some basic figures in the table below.

Representation	Stokes	$N_d = 3$	$N_d = 4$	$N_d = 5$	$N_d = 6$	$N_d = 7$
total run time	5.11s	11.52s	37.52s	51.56s	83.74s	194.01s
total number of unknowns ($\times 10^5$)	1.16	1.67	2.83	3.60	4.37	6.43
non-zeros in global matrix ($\times 10^6$)	7.19	15.62	40.59	61.37	86.98	177.37

All computations have been conducted on 16 Intel Xeon CPUs (2.67 GHz) with shared memory. If the Stokes data is taken as reference, it follows that low Knudsen simulations can be estimated with about 2- to 7-times the computational time and less than 3-times the storage requirements, while the large Knudsen number case needed up to 20 times the time and 6 times the storage. Note, that 80–90% of the run time is spend in the linear solve of the global matrix, currently based on the sparse direct solver Pardiso [25]. Obviously, the linear solve allows many possibilities of optimization, for example a multi-grid cycle through models instead of grids.

7. Conclusions

The paper presented a numerical framework for a hierarchical solution technique for the Boltzmann equation based on Hermite discretizations. The coarse representations give a valid and efficient solution the fluid dynamic equations, while finer representations allow to solve the Boltzmann equation accurately. We demonstrate the capability of the method both on simplified model problems and for realistic complex geometries in two space dimensions. It turned out that the stability of boundary conditions is essential for convergence of the numerical method especially on non-Cartesian domains.

The results of this paper follow a proof-of-concept approach such that several questions and challenges remain. Besides the obvious aspects of the numerical method, like higher order boundary elements, grid adaptivity, moving meshes, the possibility of model error estimation and m(odel)-refinement is largely left for future work. Important extensions would be time-dependency which leads to interactions of waves and dissipation like in [31], and to add nonlinear terms like convection and heat dissipation. Both time-dependency and nonlinearity would be implemented in an iterative fashion exploiting the existing implicit method for the steady linear part. Furthermore, residual-based error indicators for the model error as well as adjoint-based techniques for local model refinement can be explored.

Acknowledgements

The authors acknowledge funding of the German Research Foundation (DFG) under grant TO 414/3-1.

References

- [1] J.D. Au, M. Torrilhon, W. Weiss, The shock tube study in extended thermodynamics, *Phys. Fluids* 13 (7) (2001) 2423–2432.
- [2] L.L. Baker, N.G. Hadjiconstantinou, Variance reduction for Monte Carlo solutions of the Boltzmann equation, *Phys. Fluids* 17 (5) (2005) 051703.
- [3] G.A. Bird, *Molecular Gas Dynamics and the Direct Simulation of Gas Flows*, Clarendon Press, Oxford, 1995.
- [4] D.M. Bond, V. Wheatley, M.N. Macrossan, M. Goldsworthy, Solving the discrete S-model kinetic equations with arbitrary order polynomial approximations, *J. Comput. Phys.* 259 (2014) 175–198.
- [5] Z. Cai, R. Li, Numerical regularized moment method of arbitrary order for Boltzmann-BGK equation, *SIAM J. Sci. Comput.* 32 (5) (2010) 2875–2907.
- [6] Z. Cai, M. Torrilhon, Approximation of the linearized Boltzmann collision operator for hard-sphere and inverse-power-law models, *J. Comput. Phys.* 295 (2015) 617–643.
- [7] C. Cercignani, *The Boltzmann Equation and Its Applications*, Springer, 1988.
- [8] G. Dechrista, L. Mieussens, Numerical simulation of micro flows with moving obstacles, *J. Phys. Conf. Ser.* 362 (1) (2012) 012030.
- [9] P. Degond, G. Dimarco, L. Mieussens, A multiscale kinetic-fluid solver with dynamic localization of kinetic effects, *J. Comput. Phys.* 229 (13) (2010) 4907–4933.
- [10] F. Francis, S. Jin, A class of asymptotic-preserving schemes for kinetic equations and related problems with stiff sources, *J. Comput. Phys.* 229 (20) (2010) 7625–7648.
- [11] K.O. Friedrichs, Symmetric positive linear differential equations, *Commun. Pure Appl. Math.* 11 (3) (1958) 333–418.
- [12] I.M. Gamba, S.H. Tharkabhushanam, Spectral-lagrangian methods for collisional models of non-equilibrium statistical states, *J. Comput. Phys.* 228 (2009) 2012–2036.
- [13] C. Geuzaine, J-F. Remacle, Gmsh: a 3-d finite element mesh generator with built-in pre- and post-processing facilities, *Int. J. Numer. Methods Eng.* 79 (11) (2009) 1309–1331.
- [14] V. Girault, P.A. Raviart, *Finite Element Methods for Navier–Stokes Equations: Theory and Algorithms*, Springer, Berlin, 1986.
- [15] M.H. Gorji, M. Torrilhon, P. Jenny, Fokker–Planck model for computational studies of monatomic rarefied gas flows, *J. Fluid Mech.* 680 (2011) 574–601.
- [16] H. Grad, On the kinetic theory of rarefied gases, *Commun. Pure Appl. Math.* 2 (4) (1949) 331–407.
- [17] S.R. De Groot, P. Mazur, *Non-Equilibrium Thermodynamics*, Courier Corporation, 1984.
- [18] J.S. Hesthaven, T. Warburton, *Nodal Discontinuous Galerkin Methods*, Springer, New York, 2008.
- [19] J. Köllermeier, M. Torrilhon, Numerical study of partially conservative moment equations in kinetic theory, *Commun. Comput. Phys.* 21 (4) (2017) 981–1011.
- [20] R.J. LeVeque, *Finite Volume Methods for Hyperbolic Problems*, Cambridge University Press, 2002.
- [21] I. Müller, T. Ruggeri, *Rational Extended Thermodynamics*, 2nd edition, Springer, 1998.
- [22] J. Nordstrom, M. Svard, Well-posed boundary conditions for the Navier–Stokes equations, *SIAM J. Numer. Anal.* 43 (3) (2006) 1231–1255.
- [23] L. Pareschi, G. Russo, Numerical solution of the Boltzmann equation I: spectrally accurate approximation of the collision operator, *SIAM J. Numer. Anal.* 37 (4) (2000).

- [24] A.S. Rana, H. Struchtrup, Thermodynamically admissible boundary conditions for the regularized 13-moment-equations, *Phys. Fluids* 28 (2) (2016) 027105.
- [25] O. Schenk, K. Gärtner, Solving unsymmetric sparse systems of linear equations with PARDISO, *J. Future Gener. Comput. Syst.* 20 (3) (2004) 475–487.
- [26] C. Schmeiser, A. Zwirchmayr, Convergence of moment methods for linear kinetic equations, *SIAM J. Numer. Anal.* 36 (1999) 74–88.
- [27] H. Struchtrup, *Macroscopic Transport Equations for Rarefied Gas Flows*, Springer, 2010.
- [28] H. Struchtrup, M. Torrilhon, Regularization of Grad's 13 moment equations: derivation and linear analysis, *Phys. Fluids* 15 (9) (2003) 2668–2680.
- [29] H. Struchtrup, M. Torrilhon, H-theorem, regularization, and boundary conditions for linearized 13-moment-equations, *Phys. Rev. Lett.* 99 (2007) 014502.
- [30] T.J. Tautges, R. Meyers, K. Merkle, C. Stimpson, C. Ernst, Moab: A Mesh-Oriented Database, Sandia Reports, SAND2004(1592), 2004.
- [31] M. Torrilhon, Characteristic waves and dissipation in the 13-moment-case, *Contin. Mech. Thermodyn.* 12 (5) (2000) 289–301.
- [32] M. Torrilhon, Slow gas microflow past a sphere: analytical solution based on moment equations, *Phys. Fluids* 22 (7) (2010) 1–16.
- [33] M. Torrilhon, Convergence study of moment approximations for boundary value problems of the Boltzmann-BGK equation, *Commun. Comput. Phys.* 18 (03) (2015) 529–557.
- [34] M. Torrilhon, Modeling nonequilibrium gas flow based on moment equations, *Annu. Rev. Fluid Mech.* 48 (1) (2016) 429–458.
- [35] M. Torrilhon, J.D. Au, H. Struchtrup, Explicit fluxes and productions for large systems of the moment method based on extended thermodynamics, *Contin. Mech. Thermodyn.* 15 (1) (2003) 97–111.
- [36] M. Torrilhon, N. Sarna, GitHub repository: hierarchical Boltzmann. Source code, [www.github.com/torrilhon/HierarchicalBoltzmann](https://github.com/torrilhon/HierarchicalBoltzmann), 2016.
- [37] M. Torrilhon, H. Struchtrup, Boundary conditions for regularized 13-moment-equations for micro-channel-flows, *J. Comput. Phys.* 227 (3) (2008) 1982–2011.
- [38] A. Westerkamp, M. Torrilhon, Slow rarefied gas flow past a cylinder: analytical solution in comparison to the sphere, *AIP Conf. Proc.* 1501 (1) (2012) 207–214.